Solar Energy Materials & Solar Cells 208 (2020) 110384

Contents lists available at ScienceDirect

Solar Energy Materials and Solar Cells

journal homepage: http://www.elsevier.com/locate/solmat

Visible light-assisted instability of kesterite Cu_2ZnSnS_4: What are the implications?

Julia Kois [a], Svetlana Polivtseva [b,*], Damir Mamedov [c,d], Ali Samieipour [a], Smagul Zh Karazhanov [c,d]

[a] LLC Auramet, Kalliomäentie 1B, 02920, Espoo, Finland
[b] School of Engineering, Department of Materials and Environmental Technology, TalTech, Ehitajate Tee 5, 19086, Tallinn, Estonia
[c] MEPhI, Faculty of Physics and Technology, Department of Materials Science, Moscow, Russia
[d] Department for Solar Energy, Institute for Energy Technology, NO-2027, Kjeller, Norway

ARTICLE INFO

Keywords:
CZTS
Electrochemical
Photoactive ternary compounds
Aqueous instability
Photocorrosion
Ab initio calculations

ABSTRACT

The development of efficient photovoltaic devices utilizing durable and cost-effective materials such as CZTS and similar ones represents a big challenge. Here, the comparison of thermodynamic calculations and electrochemical experiments reveals detrimental degradation of CZTS regardless of pH values and potentials applied. Cathodic polarization yields to the full decomposition of CZTS, while anodic polarization stabilizes partly CZTS by passivation of its surface with less-active phases. The presence of water, in general, provokes the decomposition of CZTS to various undesired phases which most likely affect the device parameters. The possible mechanism for the degradation of CZTS is proposed considering its electronic structure. Certain similarities on unfavorable processes occurring with analogous materials are expected.

1. Introduction

Modern society requires alternative and cost-effective solutions in the clean energy field. This, in turn, accelerates the development and optimization of new or currently existing technologies for different functional materials and devices. For a long time, thin-film solar cells (TFSCs) have been important representatives of cost-effective and risk-less energy sources demonstrating high conversion efficiencies [1–3]. For instance, copper-indium-gallium-selenide (CIGS) TFSCs exhibited an outstanding record efficiency of 23.35% in 2019 [2], and small-area devices utilizing cadmium telluride (CdTe) technology achieved a power conversion efficiency of 22.1% [3]. Despite the undoubted advantages of CIGS and CdTe technologies, toxicity or scarcity of their constituent elements impose some restrictions to the widespread use. These issues motivate scientists to investigate alternative absorber materials [4–20].

Since the late 2000s, copper-zinc-tin-sulfide (CZTS) has received growing research interest due to its notable optoelectronic properties such as bandgap of about 1.3–1.5 eV, high absorption coefficient (10^4–10^5 cm^{-1}) in the visible spectrum, defects induced charge carries with the concentrations varying from 1.2×10^{15} to 3.1×10^{20} cm^{-3}, along with its ecological compatibility and easy-availability of constituents [9]. The listed above attributes make CZTS attractive for the replacement of CIGS or CdTe absorber layers in TFSCs [16–18]. By the recent time, the sulfur-selenium alloy CZTSSe TFSCs have already demonstrated a considerable efficiency of 12.6% [16]. Certified efficiency exceeding 13% for CZTSSe was presented by DGIST from Korea at the 9th European Kesterite Workshop in Ghent on November 28, 2018. The company Crystalsol GmbH, the owner of the patent US6488770B1, certified an efficiency of 9.7% for the CZTSSe flexible solar cell membrane technology. The latest efficiency of 9.6% has been shown for commercial solar cell panels based on CZTS monograins (https://www.crystalsol.com). These experimentally established efficiencies are still much lower than the theoretically predicted value of 32.4% for single junction CZTS cells [17].

Recent research activities have also demonstrated the applicability of CZTS materials in other photo-assisted process applications [9]. Kesterite CZTS could be implemented as a catalyst in water-splitting systems and used for direct solar-to-chemical energy conversion in photoelectrochemical (PEC) devices [10–15]. The minor success achieved in this direction clearly indicates that the development of stable catalysts represents the major challenge. The large deviation between

* Corresponding author.
E-mail address: svetlana.polivtseva@taltech.ee (S. Polivtseva).

https://doi.org/10.1016/j.solmat.2019.110384
Received 2 July 2019; Received in revised form 11 December 2019; Accepted 26 December 2019
Available online 5 January 2020

the theoretically predicted and experimentally achievable device parameters relates to the properties of CZTS that are not understood well [21].

For instance, it is generally believed that metal sulfides are stable materials. This fact enables technologists to perform many procedures (e.g. materials synthesis, layer fabrication, etching, etc.) in aqueous solutions [4–6,22–26]. However, undesired processes which might occur at photoactive semiconducting compounds in the presence of moisture are underestimated. The studies related to this point have been mostly performed for simple binary compounds [20,22], few of studies reported for ternary and quaternary metal sulfides are limited to the band alignment calculations relatively to the water redox potentials only [18–20,22–24]. The understanding of chemical/electrochemical behavior of multielement compounds like CZTS in solution-assisted processes is important from an application point of view. The knowledge of possible detrimental features occurring on the material's surface and in bulk is primarily important for further development of subsequent technologies to produce high-performance complete devices.

Considering all these aspects, we aim to study the behavior of CZTS in aqueous solutions using a systematic approach combining thermodynamic calculations and electrochemical measurements. We show that moisture modifies significantly the surface of CZTS, affects its properties and can limit the performance and durability of devices. We provide a complex understanding of mechanism for detrimental processes arising in the CZTS-water system, which is postulated to be valid not only for CZTS materials but also for other relevant PV materials.

2. Experimental

2.1. Theoretical calculation

The thermodynamic stability of CZTS at different pH values was analyzed using the *Eh-pH* (Pourbaix) diagram. The *Eh-pH* diagram was constructed employing the approach developed by Pourbaix et al. [27,28] and presented in the SI. The necessary calculations were performed fixing the equilibrium ion concentrations ([Cu] = [Sn] = [Zn] = [S]) in solution to the level of 10^{-6} mol L^{-1}, the temperature of 298 K and the pressure of 1 atm.

Electronic structure and optical properties of CZTS were studied by the Vienna ab initio simulation package (VASP) together with the potential projector augmented-wave (PAW) method [29–34]. Exchange and correlation effects were described by the Perdew-Burke-Ernzerhoff (PBE) of generalized gradient approximation as well as HSE06 hybrid functional containing a modified portion of the Fock exchange [35]. PAW-PBE pseudopotentials were employed to describe the Cu($4s^1 3d^{10}$), Zn($3d^{10}$,$4s^2$), Sn($4d^{10}5s^2 5p^2$) and S($3s^2 3p^4$) valence states. Hybrid functional was performed as proposed by Heyd-Scuseria-Ernzerhof (HSE) [36,37]. In the hybrid functional a standard value of the (short-range) Hartree-Fock exchange (25%) is mixed with a portion of PBE exchange (75%). The screening parameter of 0.25 $Å^{-1}$ is used. Structural optimization was performed with k-mesh 8 × 8 × 8, plane-wave cut-off energy of 600 eV, and energy error of 10^{-8} eV. The residual forces and pressure are less than 10^{-4} eV/A and 0.06 kB, respectively. Electronic structure calculations were used for band gap (E_g) estimations.

2.2. Preparation of CZTS monograin layer electrode

CZTS monograin powders with the elemental composition of *Cu: Zn : Sn: S* = 24.4 : 13.1 : 12.4 : 50.1 in at% were provided by Crystalsol GmbH (www.crystalsol.com, a spin-off company of Taltech). The electrode samples were prepared using the crystalline 38–45 μm fraction of Cu_2ZnSnS_4 particles (Fig. S1a) typically employed for layer-based photovoltaic modules [38]. The CZTS monograin powders were arranged as a single layer fixed by a polymer matrix open and accessible from both sides. The CZTS monograin layers (Fig. S1b) were prepared following the process described in Refs. [39,40].

CZTS monograin layers were fixed by graphite conductive adhesive (aqueous based, AlfaAesar) to the copper tape used as a back contact. The Cu type was protected from the solution using pressure-sensitive tapes (Scotch). Only one side of CZTS monograin layer was exposed to the solution. Prior to each electrochemical experiment, the electrodes were checked to ensure the absence of corrosion.

2.3. Characterization of CZTS electrodes

All electrochemical experiments and impedance measurements were performed in dark at 25 °C using a Gamry Reference 3000 potentiostat/galvanostat controlled by Gamry software. Electrochemical analysis was performed by a conventional three-electrode electrolytic cell consisting of a working CZTS monograin electrode, a platinum wire counter electrode and a reference saturated calomel electrode (SCE, +0.244 V vs. SHE at 25 °C). All electrode potentials are reported with respect to the SHE.

All electrochemical experiments were performed using 0.1 M H_2SO_4 (Fisher Scientific) solution as a background electrolyte. Before each electrochemical measurement, electrodes were immersed in the background electrolyte for 20 min to stabilize the open circuit potential (OCP) value in the range of ±10 mV. The cyclic voltammetry was applied to study the electrochemical decomposition behavior of CZTS. The sweep rate of cyclic voltammetry experiments was 20 mV s^{-1} as the essential features were evident at this rate. Electrochemical impedance spectroscopy tests were conducted at different potentials and in the frequency range of 10^{-2} – 10^{6} Hz with the peak-to-peak amplitude of 10 mV, recording 10 points per frequency decade.

For photoelectrochemical measurements, the CZTS electrodes were illuminated in electrochemical cells with light from a "white" LED lamp. The light intensity measured on the working electrode interface was around 30 mW/cm^2.

The morphological changes of obtained samples and partly the changes in elemental compositions before and after the characterization procedures were evaluated using a Zeiss Merlin scanning electron microscope (SEM) equipped with the Bruker EDX-XFlash6/30 system. The SEM and EDX measurements were performed at acceleration voltages of 4 and 10 kV, respectively. The polarographic measurements were employed to study compositions of leached solutions.

3. Result and discussion

3.1. Pourbaix diagram

Fig. 1 represents the *Eh-pH* equilibrium diagram for the Cu_2ZnSnS_4–H_2O system with marked domains of thermodynamic stability for CZTS. All the electrochemical reactions considered in this study for the CZTS decomposition are listed in Table S1. Our calculations clearly demonstrate that electrochemical oxidation and reduction of CZTS could proceed via multiple parallel processes resulting in the formation of various products explained below. As the quantities of possible redox reactions are high, the Pourbaix diagram illustrates only selected thermodynamically-favorable reduction (1–7) and oxidation (8–13) reactions (Table 1). For better readability, the plotted Pourbaix diagram for the Cu_2ZnSnS_4–H_2O system is divided into anodic (Fig. 1a) and cathodic (Fig. 1b) processes. The kinetical aspects have not been considered for the construction of this diagram.

Under anodic conditions, the domain marked by green color exhibits a plateau that corresponds to stability of CZTS at potentials of about −0.45 V vs SHE or lower in the range of pH varying from 0 to 9 (Fig. 1a). However, higher pH values in solution require more negative potentials to be applied for keeping CZTS stable. Under cathodic conditions, the CZTS stability depends on both potential applied and pH value in solution (Fig. 1b). It is important to note that the stability plateau is less pronounced compared to the anodic conditions and can be observed

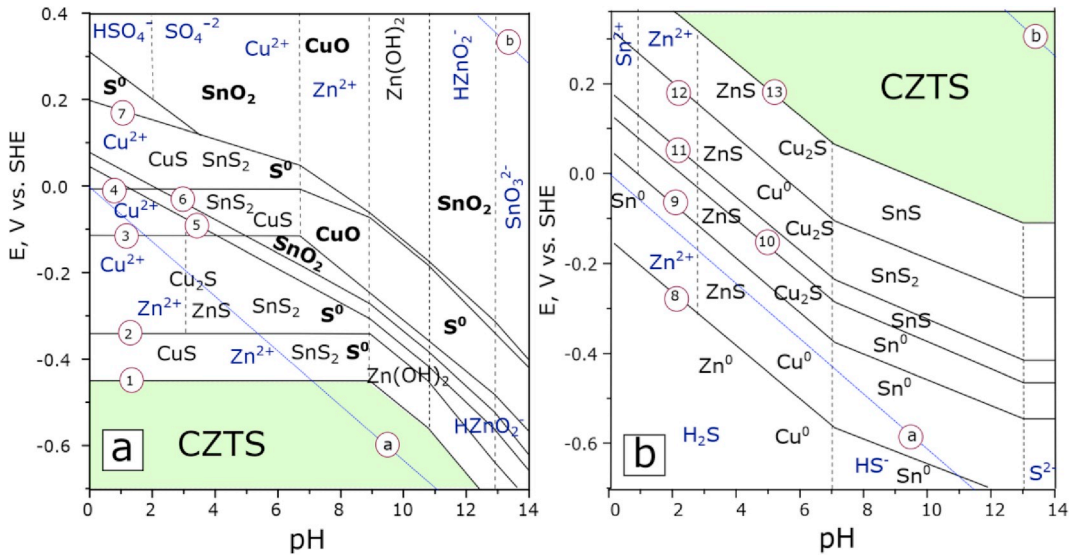

Fig. 1. Potential-pH equilibrium diagrams for a) anodic and b) cathodic reactions in the Cu_2ZnSnS_4–H_2O system. The green filled area corresponds to the stability domain of CZTS. Passivated products of reactions are designated in **bold letters**. The lines represent the equilibria between solid Cu_2ZnSnS_4 and the reaction products. The encircled numbers refer to the reactions listed in Table 1. The (a) and (b) dashed lines bound the stability region of water. (For interpretation of the references to color in this figure legend, the reader is referred to the Web version of this article.)

Table 1
The redox equilibriums and limits for the domains of relative predominance of dissolved substances in the CZTS–H_2O system.

Redox equilibria	Reaction number	Potential V *vs.* SHE[a]
$Cu_2ZnSnS_4 + 2h^+ \rightleftarrows 2CuS + Zn^{2+} + SnS_2$	1	−0.45
$Cu_2ZnSnS_4 + 2h^+ \rightleftarrows Cu_2S + Zn^{2+} + SnS_2 + S^0$	2	−0.16
$Cu_2ZnSnS_4 + 2h^+ \rightleftarrows CuS + ZnS + SnS_2 + Cu^{2+}$	3	−0.11
$Cu_2ZnSnS_4 + 4h^+ \rightleftarrows CuS + Zn^{2+} + SnS_2 + Cu^{2+} + S^0$	4	0.00
$Cu_2ZnSnS_4 + 2H_2O + 6h^+ \rightleftarrows 2CuS + Zn^{2+} + SnO_2 + 2S^0 + 4H^+$	5	0.01
$Cu_2ZnSnS_4 + 2H_2O + 6h^+ \rightleftarrows Cu_2S + Zn^{2+} + SnO_2 + 3S^0 + 4H^+$	6	0.04
$Cu_2ZnSnS_4 + 2H_2O + 10h^+ \rightleftarrows 2Cu^{2+} + Zn^{2+} + SnO_2 + 4S^0 + 4H^+$	7	0.18
$Cu_2ZnSnS_4 + 8H^+ + 8e^- \rightleftarrows 2Cu^0 + Zn^0 + Sn^0 + 4H_2S$	8	−0.21
$Cu_2ZnSnS_4 + 6H^+ + 6e^- \rightleftarrows 2Cu^0 + ZnS + Sn^0 + 3H_2S$	9	−0.01
$Cu_2ZnSnS_4 + 4H^+ + 4e^- \rightleftarrows Cu_2S + ZnS + Sn^0 + 2H_2S$	10	0.07
$Cu_2ZnSnS_4 + 4H^+ + 4e^- \rightleftarrows 2Cu^0 + ZnS + SnS + 2H_2S$	11	0.12
$Cu_2ZnSnS_4 + 2H^+ + 2e^- \rightleftarrows 2Cu^0 + ZnS + SnS_2 + H_2S$	12	0.26
$Cu_2ZnSnS_4 + 2H^+ + 2e^- \rightleftarrows Cu_2S + ZnS + SnS + H_2S$	13	0.42

[a] Corresponding redox potentials vs. SHE were calculated holding the pH value of 1, fixing the equilibrium ion concentrations in solution to the level of 10^{-6} mol L^{-1}, the temperature of 298 K and the pressure of 1 atm.

only in strongly basic solutions (pH = 13–14) at negative potentials of about −0.1 V vs. SHE and higher. In more acidic solutions (pH < 13), the stability of CZTS strongly depends on the applied potential (Fig. 1b). For instance, to retain CZTS stable at pH = 7 requires applying potentials of about +0.1 V vs. SHE or higher. Otherwise, decomposition of CZTS could occur according to the boundary lines with the formation of several by-products in obedience to the reactions explained below. Our calculations reveal the most notable feature for the behavior of CZTS in aqueous solutions. This is a lack of any extended or even point stability region (Fig. 1).

3.1.1. *Role of free electrons in bottommost conduction band in electrochemical decomposition of CZTS*

Fig. 2 represents the orbital and site projected density of states (PDOS). The analysis shows that the topmost valence band consists of two broad sub-bands. Both are strongly contributed by antibonding orbitals of Cu 3*d* hybridized with S 3*p* orbitals whereas the bottommost conduction band is contributed by antibonding orbitals of Sn 5*s* and S 3*p* electrons. The Zn and Sn atoms donate the valence electrons to S atoms and do not show states in the topmost valence band edges of both CZTS (Fig. 2). Two localized bands are available located at smaller energies of the broad Cu-derived bands. The localized band at lower energies is

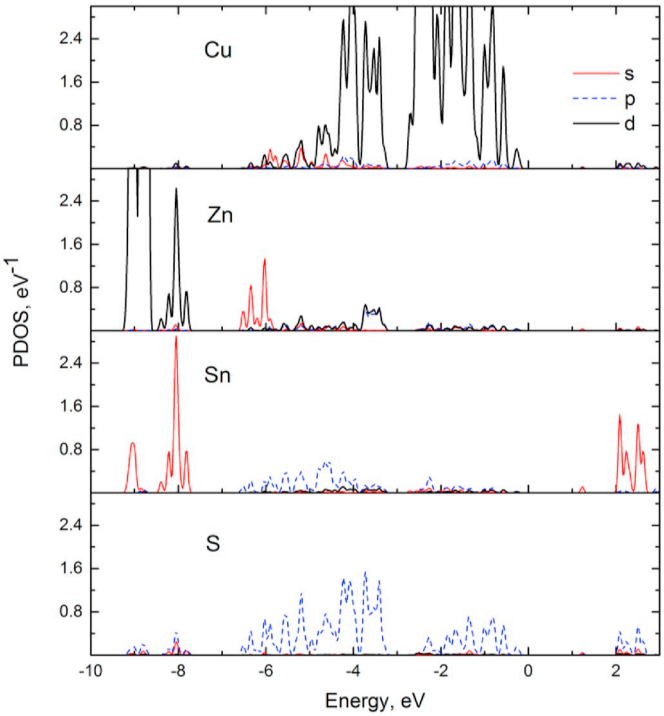

Fig. 2. Orbital and site projected density of states (PDOS) for kesterite CZTS from HSE06 calculations with mixing parameter 0.25.

mostly contributed by Zn 3*d* electrons hybridized with Sn 4*d* electrons. The analysis shows that conduction band minimum (CBM) is contributed by *s* valence states of Sn, Zn, and Cu metallic atoms. Consequently, upon electron injection into CZTS or illumination of CZTS by sunlight, free electrons will be transferred from S^{2-} anions into the above-mentioned transition metal cations that to some extent weakens chemical bonding between cations and anions and assists electrochemical decomposition of CZTS.

3.1.2. Anodic decomposition

The electrochemical oxidation is initiated by holes. The majority carriers interact with the valence band of CZTS resulting in the oxidation of Cu^{+} to Cu^{2+} and S^{2-} to highly favorable S^0 or less-favorable but still possible S^{6+}. Furthermore, the interaction of holes with CZTS increases the interatomic distance between Cu and S, and/or Zn and S atoms, which in turn enables metal cations (mostly Cu^{2+} and Zn^{2+}) to interact actively with ions or molecules in solution and to leave the CZTS lattice. Thus, at initial stages, the oxidation of CZTS can be described by the following intermediate reaction:

$$Cu_2ZnSnS_4 + (x+2z)h^{+} \rightarrow Cu_{2-x}Zn_{1-y}SnS_{4-z} + xCu^{2+} + yZn^{2+} + zS^0 \quad (14)$$

According to thermodynamic estimations, the anodic decomposition of CZTS in acidic solutions can be described by the reactions 1–4 (Fig. 1a, Table 1). The process of partial leaching of Zn^{2+} from the crystal could contribute to the formation of ternary compounds Cu_2SnS_3 on the surface of CZTS by the reaction:

$$Cu_2ZnSnS_4 + 2h^{+} \rightarrow Cu_2SnS_3 + Zn^{2+} + S^0 \quad (15)$$

In addition, the surface of CZTS can be passivated by elemental sulfur and tin(IV) oxide according to the reactions 5 and 6 (Table 1). By increasing the number of hole interactions with the CZTS valence band, the full decomposition could occur yielding the formation of completely oxidized species. Considering the solubility constants of tin(IV) products in acidic aqueous media, the formation of oxidative products can be represented by the reaction 7 (Fig. 1a, Table 1). Some authors suggest that metal sulfides can be directly oxidized to metal cations and sulfate anions under high anodic potential [26,41]. Thus, the material could be transformed to completely soluble particles by the reaction:

$$Cu_2ZnSnS_4 + 16H_2O + 36h^{+} \rightarrow 2Cu^{2+} + Zn^{2+} + Sn^{4+} + 4HSO_4^{-} + 28H^{+} \quad (16)$$

3.1.3. Cathodic decomposition

In general, the electrochemical reduction of semiconductors can be initiated by the charges donated from some external sources such as light, reducing agents and/or polarization. The electrochemical reduction of CZTS is triggered by the interaction of electrons with the valence band. At the initial stages, this leads to the changes in electronic configurations of Cu cations and reduction of Cu^{+} to Cu^0. At the later stages, the electrons can further fill the unoccupied conduction band of CZTS promoting the reduction of the other metal cations. At earlier stages, the reduction of the CZTS can be described by the following intermediate reactions:

$$Cu_2ZnSnS_4 + xH^{+} + xe^{-} \rightarrow Cu_{2-x}ZnSnS_{(4-x/2)} + xCu^0 + x/2\ H_2S \quad (17)$$

or

$$Cu_2ZnSnS_4 + xH^{+} + (x+4y)e^{-} \rightarrow Cu_{2-x}ZnSn_{1-y}S_{(4-x/2)} + xCu^0 + ySn^0 + x/2\ H_2S \quad (18)$$

Thus, according to thermodynamic calculations, the reduction of CZTS in acidic solutions could be represented by reactions 9–13 (Fig. 1b, Table 1). By increasing the number of electronic interactions with the CZTS conduction band, the reduction of Zn^{2+} cations to Zn^0 could occur resulting in full CZTS reduction according to the reaction 8 (Table 1).

Extrapolation of thermodynamic data to pH = 10–11 and OCP (Fig. S2), typical conditions for CdS fabrication using chemical bath deposition, shows that CZTS is stable for cathodic processes. However, CZTS is unstable for anodic processes at similar conditions and its surface covered by a mixture of CuO, S^0, $Zn(OH)_2$, SnO_2 and various metal sulfides (Fig. 1).

3.2. Voltammetric studies

Cyclic voltammetry measurements were carried out to investigate the oxidative and reductive reactions of CZTS in aqueous solutions. Fig. 3a shows linear-sweep voltammograms recorded for freshly polished CZTS electrode. The scan potentials were initiated from 0.6 V to −0.6 V vs. SHE in the negative directions and from 0.2 V to 1.2 V vs. SHE in the positive directions.

The peak C1 was observed at initial step cathodic decomposition at $E < 0.5$ V vs. SHE on the linear-sweep voltammogram (Fig. 3a). We could assume that the appearance of peak C1 is due to the initial cathodic dissolution of CZTS and formation of a non-stoichiometric $Cu_{2-x}ZnSnS_{4-z}$ phase by the reaction 17.

The intense mass transfer between the electrode surface and electrolyte was detected in the potential region from +0.4 to −0.1 V vs. SHE by electrochemical impedance spectroscopy (see below). The detailed description of processes corresponding to the peak C1 is complicated due to the low concentration of species formed at the interface.

Continuing potential scanning towards more negative potentials, a peak C2 may be observed at potential $-0.2 \lesssim E \lesssim 0.15$ V vs. SHE (Fig. 3a). The process associated to C2 could be described by the reaction 18. The reverse scan detects the peak at 0.34 V vs. SHE corresponding to the oxidation of Cu^0 to Cu^{2+} (see the peak A5; Fig. 3b). The newly-generated phases (reactions 9–13, Table 1) practically do not passivate the electrode surface, and the reduction potential of formed compounds is lower than the reduction potential of stoichiometric CZTS. Due to weak kinetics, it is rather difficult to segregate certain phases during the first scan. In accordance with thermodynamic calculations, the reduction of the CZTS surface to metallic tin should occur at not so high potentials. As seen in Fig. 3b, the A4 peak in the reverse scan most definitely refers to the oxidation of metallic tin.

$$SnO_2 + 4H^{+} + 4e^{-} \rightleftarrows Sn^0 + 2H_2O \quad (19)$$

At more negative potential $E \gtrsim -0.4$ V vs. SHE, a reduction process (the peak C5) associated with the decomposition of the CZTS cathode (reactions 8–9, Table 1) and the evolution of hydrogen on the CZTS cathode.

In anodic branch (Fig. 3), the small current associated to the peak A1 at potential $0.2 < E < 0.4$ V vs. SHE can represent the selective dissolution of Zn from the crystal lattice of CZTS by the reaction:

$$Cu_2ZnSnS_4 + 2xh^{+} \rightleftarrows Cu_2Zn_{1-y}SnS_{4-x} + yZn^{2+} + xS^0 \quad (20)$$

The newly-generated $Cu_2Zn_{1-y}SnS_{4-x}$ phases and elemental sulfur layer (S^0) passivate the electrode surface as the oxidation potentials of formed compounds are higher than the oxidation potential of stoichiometric CZTS. The small current (the peak A2) corresponding to the oxidation of $Cu_2Zn_{1-y}SnS_{4-x}$ to copper cations and tin oxides is observed at the anodic potential region $0.7 < E < 0.9$ V vs. SHE.

When the oxidation of CZTS is performed at $E \gtrsim 0.9$ V vs. SHE (Fig. 3), a sharp increase in current could be detected as the complete decomposition of CZTS (the peak A3) occurs along with the decomposition passivating phases on the CZTS electrode by the reaction 7 (Table 1).

To clarify different processes associated with the main peaks, we studied the effects of scan switching potentials on the current response. Fig. 3b shows the alteration in current response in the first and 10th cycles of the Cu_2ZnSnS_4 electrode after multiple cycling from −0.8 V to 1 V vs. SHE. Three appeared anodic A4, A5, A6 peaks can be associated

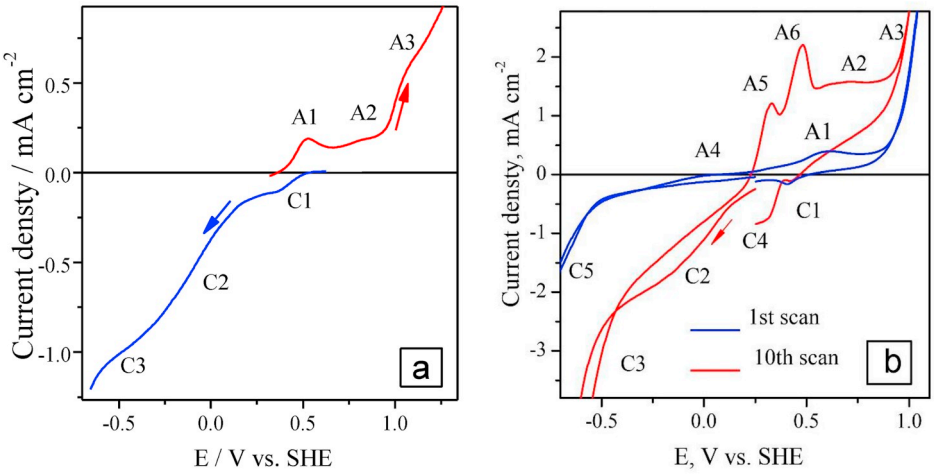

Fig. 3. a) The linear-sweep and b) the cyclic voltammograms of 1st and 10th cycles of the CZTS electrode in 0.1 M H_2SO_4 electrolyte at a sweep rate of 20 mV s^{-1}.

with the oxidation of decomposition products of CZTS. The peaks A4, A5 can be assigned to the oxidation of Cu^0 to Cu^{2+} and Sn^0 formed during the C3 and C4 processes to SnO_2 according to the reaction 19.

With a subsequent scan, the peaks A5 and C3 becomes more expressed (Figs. 3b and 4). It could be speculated that the observed effect may belong to the re-dissolution of secondary phases from the CZTS surface. The intensities of A5, A6, and C4, C6 peaks increase with the concentration of copper cations in the electrochemical solution as the result of electrochemical precipitation and dissolution of Cu^0 and various copper sulfides.

$$Cu_2S + 2H^+ + 2e^- \rightarrow 2Cu^0 + H_2S \quad (21)$$

$$CuS + Cu^{2+} + 2e^- \rightleftarrows Cu_2S \quad (22)$$

Fig. 4 shows the multi-cyclic voltammogram (10 cycles) of the CZTS electrode in the potential window of 0.4 to −0.35 V. In the first three cycles, some reduction processes (peaks C1 and C7) are observed at potentials +0.35 to −0.15 V indicating the presence of oxidation products on the CZTS surface.

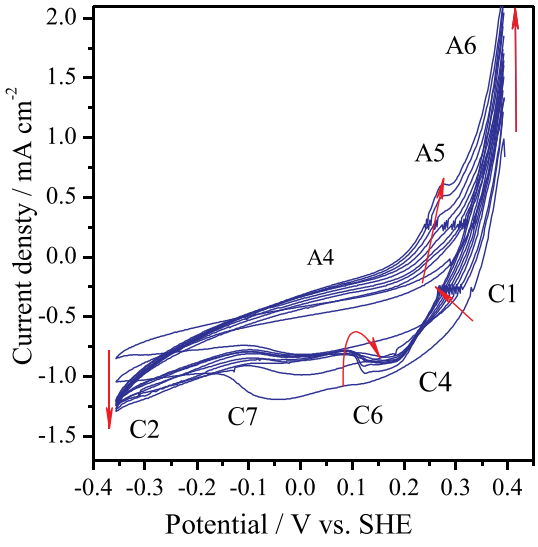

Fig. 4. Multicyclic voltammograms (10 cycles) of the CZTS electrode recorded in the potential window of from +0.40 to −0.35 V vs. SHE in 0.1 M H_2SO_4 electrolyte at a sweep rate of 20 mV s^{-1}.

3.3. Electrochemical impedance spectroscopy studies

Electrochemical impedance spectroscopy (EIS) is related to the behavior of the electrode surface/solution interface only and it was chosen to better resolve changes on the CZTS surface under polarization.

3.3.1. Cathodic polarization from -0.3V vs. SHE to OCP

Before all electrochemical measurements, electrodes were immersed in the background electrolyte for 20 min to stabilize the open circuit potential (OCP) value in the range of 0.40 ± 0.2 mV. Fig. 5a–f presents the impedance spectra recorded for the CZTS electrode under cathodic polarization from −0.3 V vs. SHE to OCP. The impedance spectra show similar behavior at low reduction potentials varying from −0.1 to 0.3 V vs. SHE (Fig. 5b–e). Three major time constants are detectable: a capacitive loop at high frequencies (400–10^5 Hz) relating to Faradaic resistance and the formation of a double layer on the CZTS electrode/surface; a second capacitive loop at middle frequencies (10–400 Hz) corresponding to the formation of a new surface layer. The straight line in the low-frequency range (10^{-2} – 10 Hz) relates to the diffusion of reduction products (H_2S) from CZTS electrode through the new surface layer to the solution and the diffusion of reactants (H^+) from the solution through the new surface layer to the CZTS surface by the reaction 18. The layer consisting of non-stoichiometric $Cu_{2-x}ZnSn_{1-y}S_{(4-x/2)}$, reduced metals and insoluble metal sulfides formed on the CZTS surface is not completely «*passive*», but rather likely to be «*pseudo-passive*». In fact, the electron charge transfer from the formed pseudo-passive layer surface is less than the electron charge transfer derived from the clean CZTS surface. Increasing the potential to −0.3 V vs. SHE shows a partially resolved semi-circle at middle frequencies, relating to the dissolution of the pseudo-passivating layer by the reaction 8 (Table 1).

The time effect of cathodic polarization at −0.15 V vs. SHE on the CZTS impedance spectrum is shown in Fig. 6a. The polarographic analysis detects the presence of H_2S in the leached solution (after 6 h treatment) and the traces of copper and tin cations due to the metal dissolution (Table S3).

The Nyquist plot shows the high-frequency loop (1 M − 20 k Hz) referring to charge transfer resistance and double layer capacitance coupling. The middle frequency impedance (20 kM–200 Hz) indicates the formation of a new surface layer on CZTS electrodes and a low frequency (1–0.1 Hz) straight line at 45° angle represented by the Warburg impedance connects to the diffusion of reacting species.

At high frequencies, a semicircle observed shows the transfer resistance slightly varying during the entire measurement period, while at low frequencies the diffusion (Warburg impedance) changes significantly over time. After 5 h of cathodic polarization, the dissipation of Warburg impedance is detected indicating a decrease in diffusion. The

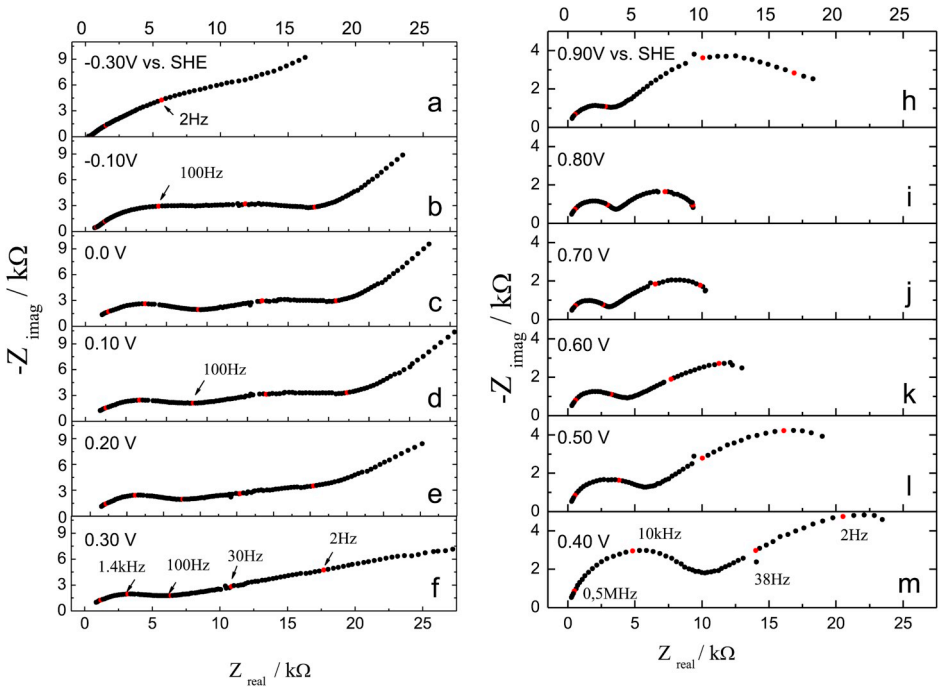

Fig. 5. Electrochemical impedance spectra of the CZTS electrode after polarization for 20 min in 0.1 M H_2SO_4 electrolyte.

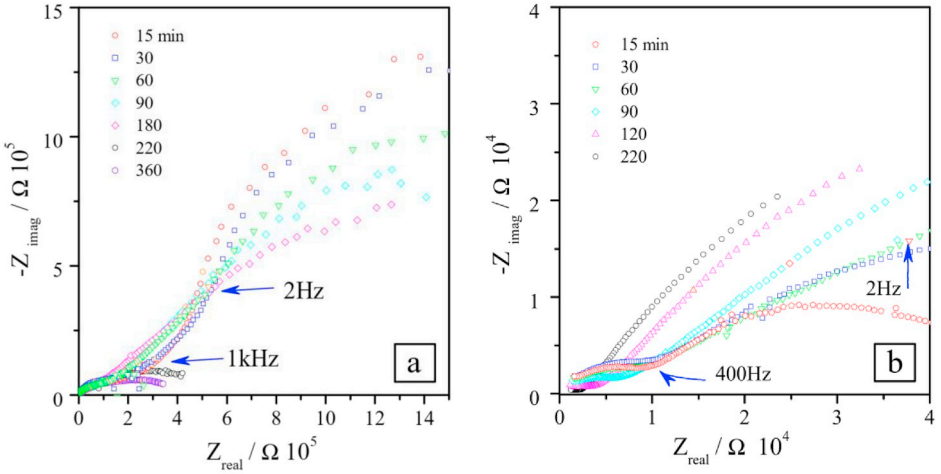

Fig. 6. Electrochemical impedance spectra of CZTS electrode recorded at (a) −0.15 V and (b) 0.6 V vs. SHE polarization in 0.1 M H_2SO_4 electrolyte.

formation of the second semicircle at low frequencies is associated with the formation of a new surface layer and the passivation of the surface by-products of CZTS decomposition.

3.3.2. *Anodic polarization from OCP to 0.9 V vs. SHE*

The impedance spectra recorded for the CZTS electrode under anodic polarization are presented in Fig. 5h-m. The impedance spectra show a capacitive two time constant at high anodic potentials varying from 0.4 to 0.9 V vs. SHE. The high-frequency impedance loop (500–10^5 Hz) is the result of charge transfer resistance and double layer capacitance coupling. As depicted in Fig. 5h-m, a depressed capacitive semicircle in the Nyquist diagram covers the middle and low-frequency region (1–500 Hz). The capacitive loop relates to the combination of a pseudo-capacitance impedance due to the presence of the passivating layer and a resistance. The diameter of the semi-circular arc relates to the stability of the passivating layer in acidic solution. As mentioned above, the oxidation of CZTS is accompanied by surface and crystal decomposition, leaching of copper and zinc from CZTS and the formation of passivating layer composing of insoluble sulfur and tin oxides tailings according to the reactions 2, 4–7, 15. It seems that more atomic layers are involved in the processes mentioned above with an increase in potentials (Fig. 5i-l). This leads to the gradual formation of the passivating layer and the growth of its thickness on the electrode surface, which in turn inhibits the CZTS dissolution. The time effect of the anodic polarization at 0.6 V vs. SHE on the impedance spectrum of CZTS is shown in Fig. 6b. The complex plane plots of CZTS polarized during the first 60 min show the passivating layer-induced pseudo-capacitance impedance at the middle (500–20 Hz) and low (0.2–10 Hz) frequencies accompanied by the Warburg diffusion impedance. After 2 h of processing, the diffusive component decreases, and the semicircles seem to be evolving into two capacitive semicircles. Since copper and zinc cations were present in the leached solution as detected by polarographic analysis (Table S3), more studies are needed to confirm the composition of the passivating layer formed on the CZTS surface.

3.4. Open circuit potential

The surface activity of the electrode immersed in 0.1 M H_2SO_4 solution was revealed by open circuit potential curves of CZTS electrodes as a function of time in Fig. 7. The OCP of all CZTS electrodes was detected close 0.25 ± 0.02 V vs. SHE in the moment of immersion. The CZTS electrode demonstrates increasing OCP for 3–7min, which reaches afterward a quasi-steady state. Herein, we defined a steady-state as a signal varied with a minor amplitude of below 2 mV/min. All the CZTS electrodes displayed the open circuit potential of 0.40 ± 0.02 V after stabilization for 10 min in the electrolyte. The rapid increase in the potential (+20 mV) observed for CZTS electrodes immersed in the electrolyte for the first 10 min indicates the spontaneous formation of the passivating layer on the surface.

Fig. 8 shows the EIS diagrams obtained for CZTS electrodes immersed in 0.1 M H_2SO_4 solution for 6 h. The complex plane plots (Fig. 8a) demonstrating a single capacitive semicircle followed by a diffusional component at low frequencies obtained for immersion time of up to 2 h. After 2 h, the semicircles seem to be evolving to two capacitive semicircles. The Bode phase diagrams (Fig. 8b) indicate the presence of at least two time-constants. One time-constant is in the medium frequency region and related to the charge transfer process involving the CZTS/solution interface. Another time-constant is in the low-frequency region and associated with the mass transfer process. The diffusion process is more pronounced during the first 2 h and seems to be neglected after that as evident from the decrease in the slope of $|Z|$ plots vs. log f (Fig. 8b).

3.5. Photoelectrochemical decomposition of CZTS

Fig. 9 demonstrates linear-sweep voltammograms measured for the CZTS electrode under chopped light illumination. The bare CZTS electrode (the first scan) exhibits a spike-like cathodic photocurrent respond (Fig. 9, black line) at potentials below +0.5 V *vs.* SHE. More negative voltages yield a gradual increase of photocurrent density to the saturated current density value of 1.5 mA cm^{-2} recorded at potentials below −0.5 V vs. SHE. After linear-sweep voltammogram measurements performed for the bare CZTS electrode, the sample was left it in electrolyte for 2 h under chopped illumination to modify the surface. The treated CZTS electrode exhibits a significant decrease by 77% of the cathodic photocurrent compared to the bare electrode value (Fig. 9, red line). The OCP is shifted to the more negative potential and the photocurrent saturation appeared at more positive potentials. The cathodic peak observed at 0.1 V vs. SHE corresponds to the reduction of formed copper sulfides on the CZTS surface (the peak C6, Fig. 4). This deterioration is attributed to the degradation of CZTS due to photocorrosion.

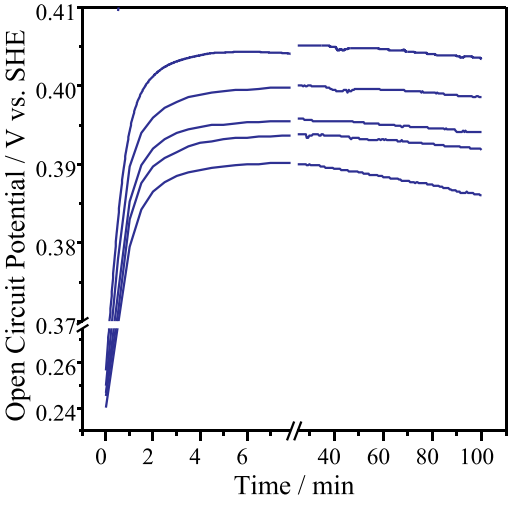

Fig. 7. Open circuit potential of different CZTS electrodes vs. time in 0.1 M H_2SO_4 solution in dark.

The OCP evolution vs. time for the CZTS electrode under chopped illumination is shown in Fig. 10. The OCP shows a negative photoresponse of about 2 mV immediately after the immersion of CZTS into the electrolyte and then it evolves to 5 mV after the treatment for 10min (Fig. 10b). Importantly, the photoresponse changes the polarity from negative to positive after the treatment for 13min. Then it gradually increases the magnitude and reaches the constant value of 15 mV after 30 min of processing (Fig. 10c). Further studies are needed to explain the observed behavior.

To simulate the effect of photocorrosion, we etched CZTS samples in 0.1 M H_2SO_4 solutions for 26 days in dark and under day-light illumination. Polarographic analysis of etched solutions reveals high contents of copper and zinc cations with the traces of tin cations (see Table S3). The SEM images of the bare and treated CZTS crystals are compared in Fig. 11. The SEM image of CZTS treated in dark show minor morphological changes after leaching (Fig. 11b). Remarkably, the day-light illumination treatment yields the formation of microrelief consisting of arranged etching pits on the CZTS surface and orientated along with some certain crystal faces (Fig. 11c and d). It should be noted that photocorrosion leads also to the appearance of very specific deep triangular pits (Fig. 11c). The shape and orientation of the formed deep pits suggest that the leaching occurs via the certain crystal planes, most probably through (011), (001), and (101) planes (See Fig. S3). Such anisotropic etching has not been previously reported for the wet-chemically or electrochemically treated CZTS materials [42]. Furthermore, the presence of micron-sized cubes of $ZnSnO_3$ (See Fig. S6) on the day-light treated CZTS surface (Fig. 11c) as confirmed by EDX shows the complexity of electrode processes for this system.

3.6. Proposed photodegradation mechanism

Considering the above-mentioned data, we present the possible photodegradation mechanism for CZTS materials. The photodecomposition starts when CZTS is bombarded with visible light irradiation, causing an electron to be ejected from filled valence band to unoccupied conduction band:

$$CZTS \xrightarrow{h\nu} CZTS\left(e^-_{CB} + h^+_{VB}\right) \quad (23)$$

The excitation leaves holes most likely in the electronic environment of S ($S^{\bullet-}$) and promotes electrons to the electronic environment of Sn (Fig. 2) leading to its reduction from Sn^{4+} to $Sn^{(4-n)+}$(where n varies from 1 to 4). The photogenerated $S^{\bullet-}$ holes at the valence band could interact with water molecules, solution species (e.g. H^+) and/or other generated radicals ($OH^{\bullet}$, $O_2^{\bullet-}$ or $HO_2^{\bullet}$) to form oxidized sulfur-containing products such as S^0 (reactions 2, 4–7) and SO_4^{2-} (See anodic decomposition). The photoexcited $Sn^{(4-n)+}$at the conduction band could be relaxed through two possible ways. The first way could involve the interaction of reduced Sn centers with constituents of water to form tin (IV) or tin (II) comprising oxides (e.g. $ZnSnO_3$). The second way belongs to the relaxation of $Sn^{(4-n)+}$from the photoexcited state to the ground one via transferring an electron to the valence band (to Cu^+ or $S^{\bullet}$) with the formation of Cu^0 or S^{2-}.

Our theoretical calculations performed clearly demonstrate that the presence of copper and tin in CZTS accelerate the possible detrimental reactions (Fig. 2). Furthermore, the interaction of CZTS with chopped illumination could lead to the formation of unstable Cu_2SO_4 in the system as Cu(I) cations are available on the CZTS surface and SO_4^{2-} anions are present in solution or can be generated through the oxidation of $S^{\bullet-}$. Considering this and the polarographic data (Table S3) along with the presence of tunnel-type micro defects in CZTS (Fig. 11c and d), we could speculate that Cu_2SO_4 formed on CZTS decomposes with the forming soluble copper compounds according to the reaction:

$$Cu_2SO_4 \rightarrow Cu^0 + CuSO_{4(aq)} \quad (24)$$

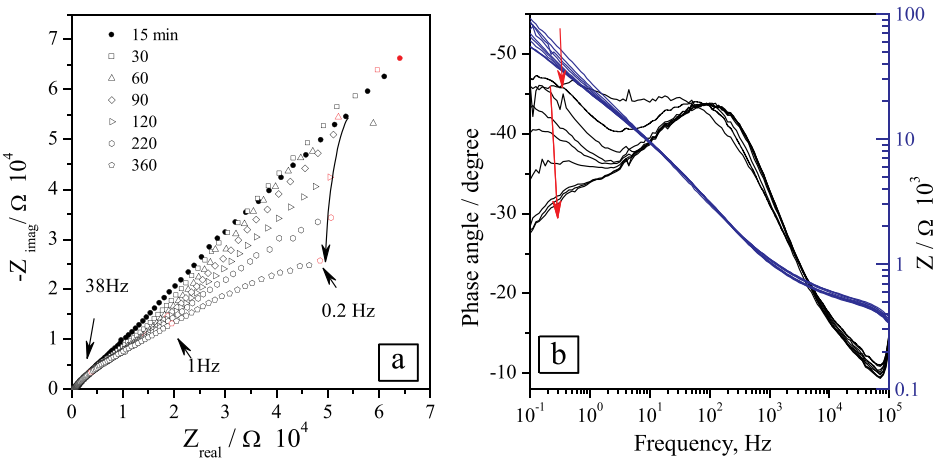

Fig. 8. Effect of OCP polarization on the CZTS electrode a) Nyquist plots, b) phase angle [Θ] and absolute impedance [Z] vs. frequency.

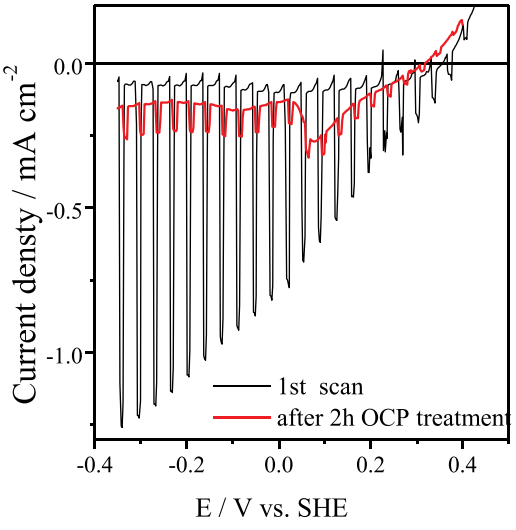

Fig. 9. Current-potential characteristics for CZTS in 0.1 M H_2SO_4 electrolyte under chopped illumination (a sweep rate of 20 mV s^{-1}).

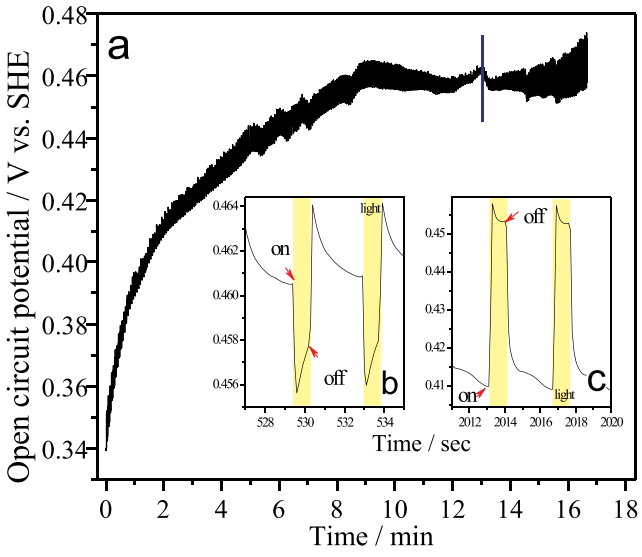

Fig. 10. (a) The time evolution for the OCP of the CZTS electrode under chopped illumination. The enlarged OCP plots ranging (b) from 527s to 535s and (c) from 2011s to 2020s for a better exhibition of a potential transient.

It should be also noted that the excitation could leave holes in the electronic structure of Cu (Cu^{2+}) (Fig. 2). Thus, an alternative way for photodegradation could occur via the formed Cu^{2+} centers in CZTS, which can be easily solvated and leached by H_2O. Although, we consider this alternative way as less likely compared to the decomposition of Cu_2SO_4. We assume that the orientated degradation presented in Fig. 11 requires available the listed above metallic atoms executively located on some specific CZTS planes. We evaluated all the crystal planes. We believe that the decoupling process will be preferably defined in the (011), (001), and (101) planes as they satisfy this assumption (Fig. S3). Considering the data presented above, the degradation mechanism for CZTS in wet-chemical systems is schematically shown in Fig. 12.

4. Conclusions

Thus, we studied the behavior of CZTS in aqueous solutions. By comparing the results in dark and under illumination with sunlight we reported about the instability of CZTS in aqueous solutions combined by the influence of visible light and trends in electrochemical decomposition. We demonstrated that CZTS is more stable under anodic polarization as the passivating layer is formed on the surface, while under cathodic polarization CZTS tends to full decomposition. We evaluated thermodynamic stability of CZTS at different pH values and potentials applied and designed the Pourbaix diagram. Based on electronic structure studies, we proposed the mechanism of decomposition of CZTS in aqueous solutions. We showed that CZTS is unstable in aqueous solutions and tends to decompose to more stable phases such as copper and tin sulfides and oxides. The mechanism is postulated to be valid for processes taking place at the surface of similar materials. The mechanism is expected to be valid also for electron-hole injection into CZTS. The results showed indication to a strong impact of environmental moisture and moisture in precursor solutions as one of the important degradation pathways of CZTS that limit the performance of devices and durability.

Author contribution statement

Julia Kois: Methodology, Investigation, Visualization, Writing-Original draft preparation. Svetlana Polivtseva: Conceptualization, Data curation, Methodology, Writing- Original draft preparation, Writing-Reviewing and Editing. Damir Mamedov: Investigation, Software, Visualization. Ali Samieipour: Investigation. Smagul Zh. Karazhanov: Software, Validation, Writing- Reviewing and Editing.

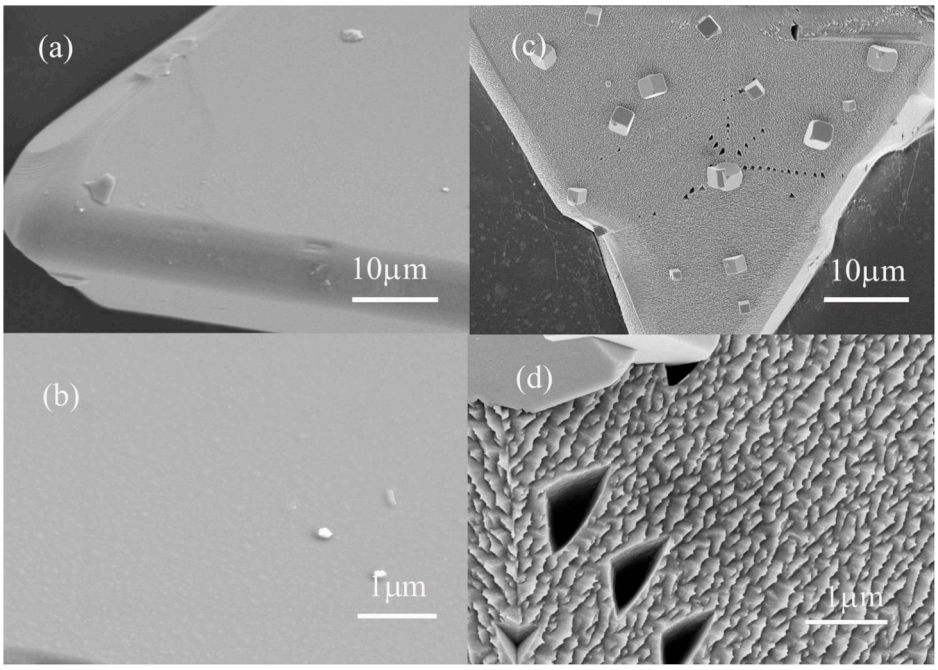

Fig. 11. SEM images of CZTS samples a) bare, b) etched in 0.1 M H_2SO_4 during 26 days in dark and c), d) under day-light illumination.

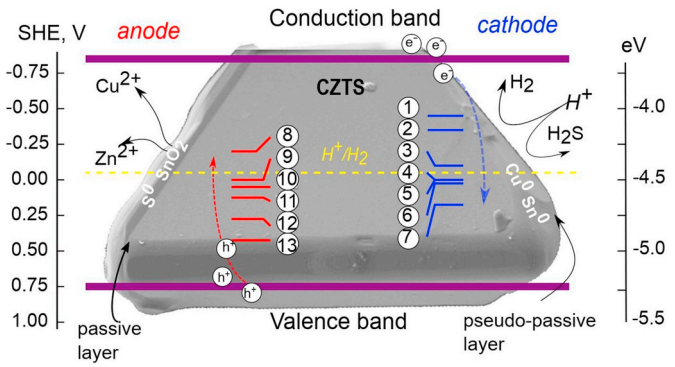

Fig. 12. Proposed decomposition mechanism for CZTS in the Cu_2ZnSnS_4–H_2O system. The encircled numbers refer to the reactions listed in Table 1.

Table of contents

Cost-effective photoactive materials demand stability and durability for photovoltaic applications. The authors report about the instability of ternary compounds like CZTS in the presence of water. Through the electronic structure of CZTS, the mechanism for decomposition is discussed, essential for designing and further improvements in technological aspects, which affect the device properties.

Declaration of competing interest

The authors declare that they have no known competing financial interests or personal relationships that could have appeared to influence the work reported in this paper.

Acknowledgments

This research was supported by the institutional research funding IUT19-28 and PUT1495 Project of the Estonian Ministry of Education and Research, the European Union through the European Regional Development Fund project "Center of Excellence" TK141 "Advanced materials and high-technology devices for sustainable energetics, sensorics and nanoelectronics", M-ERA.net project 272806. Computational work has been performed by using the Norwegian NOTUR supercomputing facilities through the project nn4608 k. The authors would like to thank Dr. Dieter Meissner, TalTech, and Crystalsol OÜ for enabling initial investigations in his group and providing CZTS monograin materials.

Appendix A. Supplementary data

Supplementary data to this article can be found online at https://doi.org/10.1016/j.solmat.2019.110384.

References

[1] J. Poortmans, V. Arkhipov, Thin Film Solar Cells Fabrication, Characterization and Applications, Wiley, Chichester, 2006.
[2] Solar Frontier press release solar Frontier achieves world record thin-film solar cell efficiency of 23.35%. http://www.solar-frontier.com/eng/news/2019/0117_press.html.
[3] M.A. Green, Y. Hishikawa, W. Warta, et al., Solar cell efficiency tables (version 50), Prog. Photovolt. Res. Appl. 25 (2017) 668–676.
[4] S. Polivtseva, I. Oja Acik, M. Krunks, K. Tõnsuaadu, A. Mere, Thermoanalytical study of precursors for tin sulfide thin films deposited by chemical spray pyrolysis, J. Therm. Anal. Calorim. 121 (2015) 177–185.
[5] S. Polivtseva, I. Oja-Acik, A. Katerski, A. Mere, V. Mikli, M. Krunks, Tin sulfide films by spray pyrolysis technique using L-cysteine as a novel sulfur source, Phys. Status Solidi C 13 (2016) 18–23.
[6] J. Kois, S. Polivtseva, S. Bereznev, The cost-effective deposition of ultra-thin titanium (IV) oxide passivating layers for improving photoelectrochemical activity of SnS electrodes, Thin Solid Films 671 (2019) 152–156.
[7] Z. Li, X. Liang, G. Li, H. Liu, H. Zhang, J. Guo, J. Chen, K. Shen, X. San, W. Yu, Y. Mai, 9.2%-Efficient core-shell structured antimony selenide nanorod array solar cells, Nat. Commun. 10 (2019) 125.
[8] N. Spalatu, J. Hiie, R. Kaupmees, O. Volobujeva, J. Krustok, I. Oja-Acik, M. Krunks, Post-deposition processing of SnS thin films and solar cells: prospective strategy to obtain large, sintered and doped SnS grains by recrystallization in the presence of a metal halide flux, ACS Appl. Mater. Interfaces 11 (2019) 17539–17554.
[9] S. Chen, A. Walsh, X.G. Gong, S.H. Wei, Classification of lattice defects in the kesterite Cu_2ZnSnS_4 and $Cu_2ZnSnSe_4$ earth-abundant solar cell absorbers, Adv. Mater. 25 (2013) 1522–1539, https://doi.org/10.1002/adma.201203146.
[10] Y. Chen, Z. Qin, T. Chen, J. Su, X. Feng, M. Liu, Optimization of $(Cu_2Sn)_xZn_{3(1-x)}S_3$/CdS pn junction photoelectrodes for solar water reduction, RSC Adv. 6 (2016) 58409–58416, https://doi.org/10.1039/C6RA22895J.

[11] G.K. Gupta, A. Dixit, Room temperature electrical properties of solution derived p-type Cu_2ZnSnS_4 thin films, AIP Conference Proceedings 1728 (2016), https://doi.org/10.1063/1.4946729, 020678.

[12] L. Rovelli, S.D. Tilley, K. Sivula, Optimization and stabilization of electrodeposited Cu_2ZnSnS_4 photocathodes for solar water reduction, ACS Appl. Mater. Interfaces 5 (2013) 8018–8024. https://pubs.acs.org/doi/10.1021/am402096r.

[13] N. Guijarro, M.S. Prevot, K. Sivula, Enhancing the charge separation in nanocrystalline Cu_2ZnSnS_4 photocathodes for photoelectrochemical application: the role of surface modifications, J. Phys. Chem. Lett. 5 (2014) 3902–3908. https://pubs.acs.org/doi/abs/10.1021/jz501996s.

[14] X. Yu, et al., Cu_2ZnSnS_4 nanocrystals as highly active and stable electrocatalysts for the oxygen reduction reaction, J. Phys. Chem. C 120 (2016) 24265–24270.

[15] S. Lu, H. Yang, F. Li, Y. Wang, S. Chen, G. Yang, Y. Liu, X. Zhang, Element substitution of kesterite Cu_2ZnSnS_4 for efficient counter electrode of dye-sensitized solar cells, Sci. Rep. 8 (2018) 8714.

[16] W. Wang, D.B. Mitzi, et al., Device characteristics of CZTSSe thin-film solar cells with 12.6% efficiency, Adv. Energy Mater 4 (2014) 1301465, https://doi.org/10.1002/aenm.201301465.

[17] W. Ki, H.W. Hillhouse, Earth-abundant element photovoltaics directly from soluble precursors with high yield using a non-toxic solvent, Adv. Energy Mater. 1 (2011) 732–735.

[18] D. Liu, D. Han, M. Huang, X. Zhang, T. Zhang, Theoretical study on the kesterite solar cells based on $Cu_2ZnSn(S,Se)_4$ and related photovoltaic semiconductors, Chin. Phys. B 27 (2018), https://doi.org/10.1088/1674-1056/27/1/018806, 018806.

[19] M.K. Gonce, M. Dogru, E. Aslan, F. Ozel, I.H. Patir, M. Kus, M. Ersoz, Photocatalytic hydrogen evolution based on Cu_2ZnSnS_4,$Cu_2ZnSnSe_4$, $Cu_2ZnSnSe_{4-x}S_x$ nanofibers, RSC Adv. 5 (2015) 94025–94028.

[20] S. Chen, L.W. Wang, Thermodynamic oxidation and reduction potentials of photocatalytic semiconductors in aqueous solution, Chem. Mater. 24 (2012) 3659–3666. https://pubs.acs.org/doi/10.1021/cm302533s.

[21] A. Redinger, D.M. Berg, P.J. Dale, S. Siebentritt, The consequences of kesterite equilibria for efficient solar cells, Am. Chem. Soc. 133 (2011) 3320–3323.

[22] L.J. Guo, J.W. Luo, T. He, S. Wei, S. Li, Photocorrosion-limited maximum efficiency of solar photoelectrochemical water splitting, Phys. Rev. Appl. 10 (2018), 064059.

[23] N. Ghamarian, Z. Zainal, M. Zidan, W.T. Tan, Photocorrosion of $CuInSe_2$ thin film by electrochemical polarization in acidic and alkaline medium, Int. J. Electrochem. Sci. 8 (2013) 5161–5171.

[24] A. Giaccherini, G. Montegrossi, F. Di Benedetto, Stability of naturally relevant ternary phases in the Cu–Sn–S system in contact with an aqueous solution, Minerals 6 (2016) 79, https://doi.org/10.3390/min6030079.

[25] A. Ghahremaninezhad, E. Asselin, D.G. Dixon, Electrochemical evaluation of the surface of chalcopyrite during dissolution in sulfuric acid solution, Electrochim. Acta 55 (2010) 5041–5056.

[26] D. Bevilaqua, et al., Effect of Na-chloride on the bioleaching of a chalcopyrite concentrate in shake flasks and stirred tank bioreactors, Hydrometallurgy 138 (2013) 1–13.

[27] M. Pourbaix, Atlas of Electrochemical Equilibria in Aqueous Solutions, National Association of Corrosion Engineers, Houston, Texas, 1974.

[28] J. Horvath, M. Novak, Potential/pH equilibrium diagram of some Me-S-H_2O ternary systems and their interpretation from the point of view of metallic corrosion, Corros. Sci. 4 (1964) 159–178, https://doi.org/10.1016/0010-938X(64)90016-2.

[29] G. Kresse, J. Furthmüller, Efficient iterative schemes for ab initio total-energy calculations using a plane-wave basis set, Phys. Rev. B. 54 (1996) 11169–11186.

[30] G. Kresse, J. Furthmüller, J. Efficiency of ab-initio total energy calculations for metals and semiconductors using a plane-wave basis set, Comput. Mater. Sci. 6 (1996) 15–50.

[31] G. Kresse, J. Hafner, Ab Initio molecular-dynamics simulation of the liquid-metal amorphous-semiconductor transition in germanium, Phys. Rev. B. 49 (1994) 14251–14269.

[32] G. Kresse, D. Joubert, From ultrasoft pseudopotentials to the projector augmented-wave method, Phys. Rev. B. 59 (1999) 1758–1775.

[33] G. Kresse, J. Hafner, Ab initio molecular dynamics for liquid metals, Phys. Rev. B. 47 (1993) 558–561.

[34] P.E. Blochl, Projector augmented-wave method, Phys. Rev. B. 50 (1994) 17953–17979.

[35] J.P. Perdew, K. Burke, M. Ernzerhof, M. Generalized gradient approximation made simple, Phys. Rev. Lett. 77 (1996) 3865–3868.

[36] A.V. Krukau, et al., Influence of the exchange screening parameter on the performance of screened hybrid functionals, J. Chem. Phys. 125 (2006) 224106, https://doi.org/10.1063/1.2404663.

[37] J. Heyd, G.E. Scuseria, M. Ernzerhof, Hybrid functionals based on a screened Coulomb potential, J. Chem. Phys. 118 (2003) 8207.

[38] E. Mellikov, M. Altosaar, M. Kauk-Kuusik, Growth of CZTS-based monograins and their application to membrane solar cells, in: K. Ito (Ed.), Copper Zinc Tin Sulfide-Based Thin-Film Solar Cells, John Wiley & Sons, 2015, pp. 289–309 (Chapter 13).

[39] A. Samieipour, E. Kouhiisfahani, S. Galajev, D. Meissner, CZTS Monograin Membranes for Photoelectrochemical Fuel Production Modifications for Fuel Production, ICCEP, 2015, pp. 212–215.

[40] E. Kouhiisfahani, A. Samieipour, T. Morawietz, J. Kraut, R. Hiesgen, D. Meissner, CZTS Monograin Membranes for Photoelectrochemical Fuel Production Modifications for Fuel Production, ICCEP), 2015, pp. 222–225.

[41] M. Bojinov, T. Tezvetkoff, The influence of solution anion on the mechanism of transpassive dissolution of ferrous- and nickel-based alloys, J. Phys. Chem. B 107 (2003) 5101–5112.

[42] K. Timmo, M. Altosaar, J. Raudoja, M. Grossberg, M. Danilson, O. Volobujeva, E. Mellikov, Chemical etching of $Cu_2ZnSn(S,Se)_4$ monograin powder, IEEE Photovol Spec Conf (2010), https://doi.org/10.1109/PVSC.2010.5616411.